Available online at www.sciencedirect.com
ScienceDirect
Journal of Power Sources 174 (2007) 114–123
JOURNAL OF POWER SOURCES
www.elsevier.com/locate/jpowsour

Grain boundary conductivity of high purity neodymium-doped ceria nanosystem with and without the doping of molybdenum oxide

J.X. Zhu [a], D.F. Zhou [a,*], S.R. Guo [c], J.F. Ye [a], X.F. Hao [b], X.Q. Cao [b], J. Meng [b,*]

[a] *School of Biological Engineering, Changchun University of Technology, Changchun 130012, China*
[b] *Key Laboratory of Rare Earth Chemistry and Physics, Changchun Institute of Applied Chemistry, Chinese Academy of Sciences, Changchun 130022, China*
[c] *Division of Nanomaterials & Chemistry, Hefei National Laboratory for Physical Sciences at Microscale, University of Science and Technology of China, Hefei 230026, China*

Received 9 July 2007; received in revised form 29 August 2007; accepted 30 August 2007
Available online 4 September 2007

Abstract

Solid solutions of $Ce_{1-x}Nd_xO_{2-x/2}$ ($0.05 \le x \le 0.2$) and $(Ce_{1-x}Nd_x)_{0.95}Mo_{0.05}O_{2-\delta}$ ($0.05 \le x \le 0.2$) have been synthesized by a modified sol–gel method. Both materials have very low content of SiO_2 (~27 ppm). Their structures and ionic conductivities were characterized by X-ray diffraction (XRD), field-emission scanning electron microscopy (FESEM) and electrochemical impedance spectroscopy (EIS). The XRD patterns indicate that these materials are single phases with a cubic fluorite structure. The powders calcined at 300 °C with a crystal size of 5.7 nm have good sinterability, and the relative density could reach above 96% after being sintered at 1450 °C. With the addition of MoO_3, the sintering temperature could be decreased to 1250 °C. Impedance spectroscopy measurement in the temperature range of 250–800 °C indicates that a sharp increase of conductivity is observed when a small amount of Nd_2O_3 is added into ceria, of which $Ce_{0.85}Nd_{0.15}O_{1.925}$ (15NDC) shows the highest conductivity. With the addition of a small amount of MoO_3, the grain boundary conductivity of 15NDC at 600 °C increases from 2.56 S m^{-1} to 5.62 S m^{-1}.
© 2007 Elsevier B.V. All rights reserved.

Keywords: Solid oxide fuel cell; Electrolyte; Grain boundary conductivity; Sol–gel method

1. Introduction

Solid oxide fuel cells (SOFCs) have been considered as power generation devices in the future as they have demonstrated high energy-conversion efficiency, high power density and extremely low pollution, in addition to flexibility in using hydrocarbon fuels. This application typically requires conduction of oxygen ions which narrows the candidate materials to solid oxide electrolytes [1]. Several investigations have focused on cubic fluorite structured oxides due to their relatively open structure [2]. The most successful fluorite-structured oxide electrolytes are those based on group IVB oxides (i.e. ZrO_2, HfO_2, CeO_2 or ThO_2) with additions of either alkaline-earth oxides (i.e. CaO or SrO) or rare-earth oxides [3]. So far, yttria-stabilised zirconia (YSZ) has been mainly used as the solid oxide electrolyte for such fuel cells because of its nearly pure oxygen ionic conductivity in an oxidizing or a reducing atmosphere and good mechanical properties. However, high operation temperatures above 900 °C are required for this electrolyte due to its relatively low oxygen-ion conductivity. This condition increases the fabrication cost and accelerates degradation of the fuel-cell system. Ceria-based solid solutions have higher oxygen-ion conductivity than YSZ at intermediate temperatures (500–700 °C) and have been regarded as the most promising electrolytes for intermediate temperature SOFC (IT-SOFC) [4].

The ionic conductivities of ceria-based electrolytes doped with various cations (e.g. Ca^{2+}, Sr^{2+}, Y^{3+}, La^{3+}, Nd^{3+}, Gd^{3+} and Sm^{3+}) at different doping concentrations have been extensively studied. However, the results reported in those works were generally dispersed, and even the same author reported contradictory results [5]. To interpret such dispersions in experimental results, it was invoked that grain boundaries probably play an important role in the electrical conductivity. Riess et al. [6] clearly demonstrated that the ionic conductivity of $(CeO_2)_{0.82}(Gd_2O_3)_{0.18}$ was strongly dependent on the preparation route. The resistance of

* Corresponding authors. Tel.: +86 431 85262030; fax: +86 431 85698041.
E-mail addresses: defengzhou65@126.com (D.F. Zhou), jmeng@ciac.jl.cn (J. Meng).

0378-7753/$ – see front matter © 2007 Elsevier B.V. All rights reserved.
doi:10.1016/j.jpowsour.2007.08.093

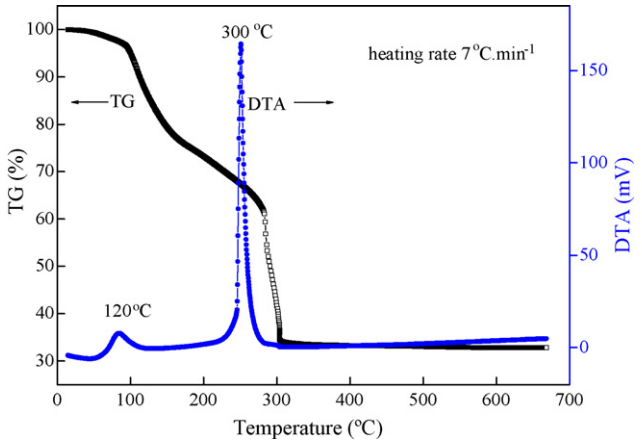

Fig. 1. TG–DTA curves of the as-dried precursor of 10NDC with a heating rate of 7 °C min^{-1} in air.

grain boundaries was found to be greater than that of the grain core, especially at low temperatures. This fact was ascribed to the presence of amorphous insulating phases in these boundaries.

The total conduction of polycrystalline electrolytes consists of both the grain boundary (GB) and grain interior (GI) conductivities. It is well known that the effect of GB conduction on the performance of electrolyte is very significant for intermediate and lower temperature applications. Besides, almost all electrolytes used in various electrochemical devices are polycrystalline. Therefore, knowledge on the properties of grain boundaries is of great importance. The GB effects have been mainly attributed to the space-charge layer [7–9] and the resistive siliceous film [10–13]. For high purity materials (SiO_2 <50 ppm) [9,14,15], GB behavior is mainly attributed to the intrinsic space-charge layer effect, since the blocking effect of siliceous phase is negligible [11,15]. The deleterious GB behavior arising from SiO_2 impurity has been recognized in zirconia-based electrolytes for several decades and in ceria-based ceramics for over 10 years. And recently, the grain boundary performance of the transition oxide-doped GDC high pure or impure systems has been systematically investigated [16–23], while much less information is available about Nd_2O_3-doped CeO_2 (NDC) system mentioning the SiO_2 content, although some literature data are available regarding the ionic conductivities as a function of dopant contents [24–26]. It is, therefore, necessary to prepare high purity NDC solid solutions and investigate the electrical conductivity of this system. Chen and Chen [27,28] have systematically studied the grain boundary diffusion of CeO_2 with addition of some transition oxides (TiO_2, Nb_2O_5 and ZrO_2).

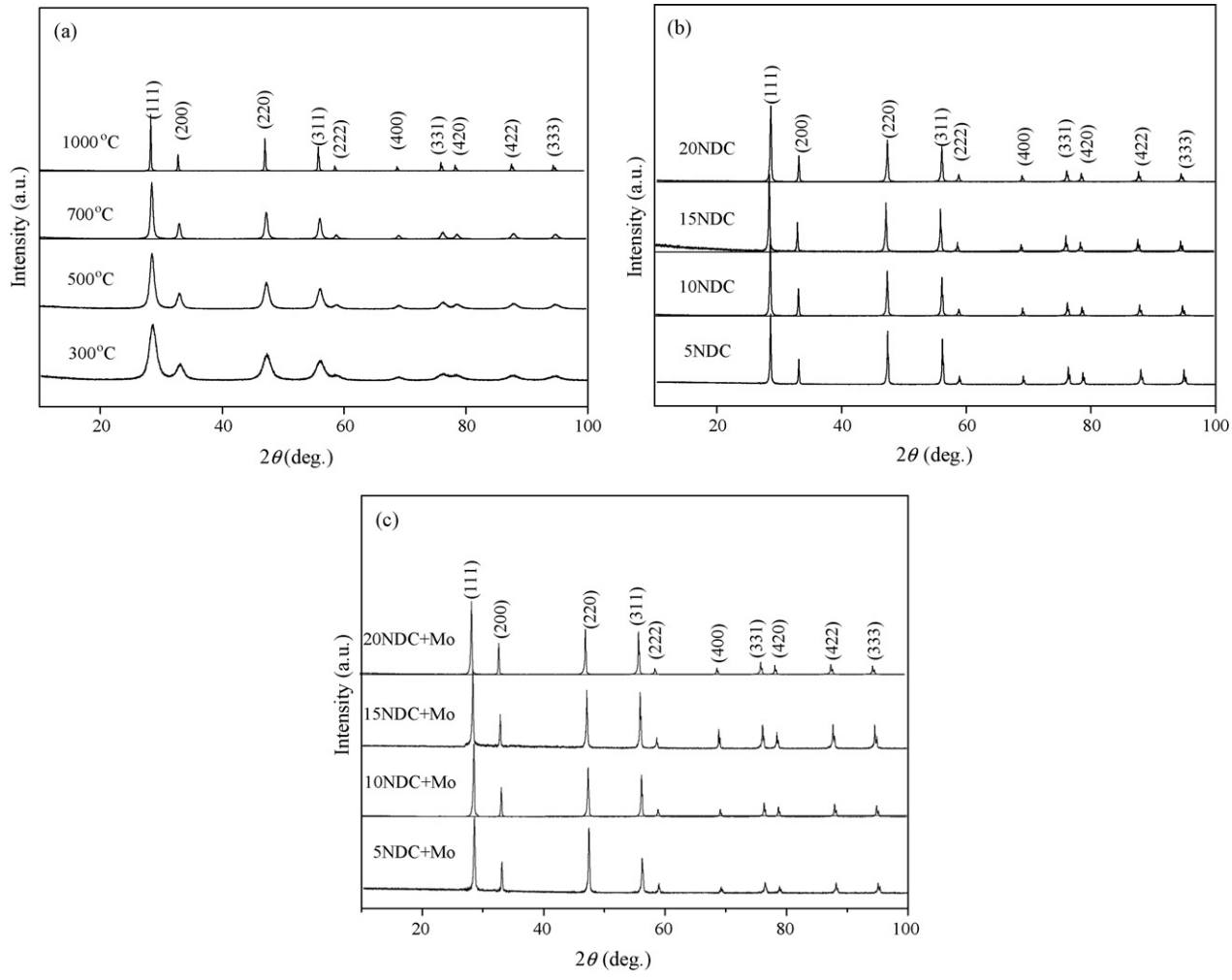

Fig. 2. (a) XRD patterns of phase evolution of 10NDC precursor powder; (b) XRD patterns of NDC without Mo doping; (c) with Mo doping sintered at 1450 °C.

They found that severely undersized dopants had a tendency to enhance markedly the grain boundary mobility. Obviously, much attention should be paid to the dopants with small ion size. Here, MoO_3 is chosen as a sintering promoter due to the small ionic size of Mo^{6+}. In this work, we have prepared high purity NDC solid solutions and systematically investigated the electrical conductivity of these ceria-based compounds. The effects of MoO_3 doping on densification and conductivity of this system have been discussed in detail.

2. Experimental

Neodymium-doped ceria with and without molybdenum doping were prepared by a modified sol–gel method as reported in Refs. [29,30]. Analytical reagents $Ce(NO_3)_3{\cdot}6H_2O$ (≥99.5%), Nd_2O_3 (≥99.999%), $C_6H_8O_7{\cdot}H_2O$ (≥99.5%) and $(NH_4)_6Mo_7O_{24}{\cdot}6H_2O$ (≥99.5%) were used as the starting materials. The molar ratio of the metal ions to citric acid was 1:1.5. Stoichiometric amounts of $Ce(NO_3)_3{\cdot}6H_2O$, $(NH_4)_6Mo_7O_{24}{\cdot}6H_2O$ and Nd_2O_3 were dissolved in the distilled water or nitric acid to form solutions, separately, and mixed them. Then solid citric monohydrate was added into the mixture with stirring at 60 °C. The transparent solution was vaporized overnight by water bath at 60 °C, resulting in a dry gel. The precursors were calcined at 300 °C for 4 h. The powder calcined at 300 °C exhibited a single phase of fluorite structure like pure CeO_2 with average particle size of 5.7 nm. SiO_2 content of the powder, which was analyzed by means of inductively coupled plasma mass spectroscopy (Plasma-Spec-1), was about 27 ppm. After pre-calcination, the precursors were ball-milled and pressed into pellets under 70 MPa followed by sintering at 1450 °C for 24 h with Pt plate as the sample holder. Densities of the sintered pellets were determined by Archimedean method.

DTA/TG were carried out on SDT 2960 (TA instruments) in the temperature range of 20–700 °C with a heating rate of 7 °C min^{-1} in air. The X-ray diffraction (XRD) patterns were recorded on a Rigaku D/max-IIB X-ray diffractometer with Cu $K\alpha_1$ radiation ($\lambda = 0.15405$ nm) at room temperature. Lattice constants of the NDC solid solutions were determined by using the Rietveld method, and crystal sizes of the oxide powders were estimated by the broadening of X-ray peak performed on the [1 1 1], [2 0 0], [2 2 0] and [3 1 1] diffraction peaks using Scherrer's equation [31]. Particle morphology, agglomeration state and crystal structure of the synthesized powders and pellets were observed via field-emission scanning electron microscopy FESEM (JXA 6400, JEOL, Japan) equipped with an energy-dispersive X-ray spectrometer (EDX) analyzer (XP30, Philips). The powder calcined at 700 °C was ultrasonically dispersed into ethanol, and the suspension was spread on the surface of a Si single crystal substrate. The pellets of the samples were polished and then thermally etched at a temperature which was 100 °C lower than the sintering temperature prior to the FESEM observation. Crystal sizes were measured from FESEM micrographs of the etched samples by using the linear intercept technique described by Mendelson [32]. The average crystal size, D, was obtained from the relation $D = 1.56L$, where L is the average grain boundary intercept length of a series of random lines on the FESEM micrographs. Oxide ionic conductivity was analyzed by electrochemical impedance spectroscopy with a frequency response analyzer (Solatron 1255) and an electrochemical interface (SI1287). Silver electrodes were coated on both sides of the pellets and heated at 550 °C for 30 min. Impedance measurement was conducted on cooling from 800 °C to 250 °C in a frequency range from 1 MHz to 0.1 Hz with an increment of 50 °C. Curve fitting and resistance calculation were done by Zview 2.1 software, using the expression of $\sigma = L/RS$, where L is the sample thickness and S is the electrode area of the sample surface.

3. Results and discussion

3.1. Structural characteristics of the powders

The thermal decomposition behavior of the as-dried precursor of $Ce_{0.9}Nd_{0.1}O_{1.95}$ (10NDC) was studied by DTA/TG, and the result was shown in Fig. 1. The total weight loss was about 67%. The exothermic peak at 120 °C with a mass loss of 15% can be attributed to the evaporation of water and decomposition of citrate or citric acid monohydrate. The other exothermic peak at 300 °C accompanied by a weight loss of 52% indicates that the decomposition occurs around 300 °C. No remarkable change could be detected above 300 °C, suggesting that the single phase of sample is formed at 300 °C, and this was confirmed by XRD (Fig. 2).

Fig. 2a shows XRD patterns of 10NDC specimen which were heated at 300 °C, 500 °C, 700 °C and 1000 °C, respectively. It is obvious that the precursor keeps the cubic fluorite-type structure at relatively low temperature (300 °C), indicating that the formation temperature of 10NDC is as low as 300 °C, which is in good agreement with the results of DTA/TG. It is noteworthy that the XRD peaks calcined at 300 °C are broad, suggesting the presence of nanometer scale particles. The peaks gradually sharpen with the increase of sintering temperature which can be attributed to the increase of crystal size. The crystal sizes of the powders calculated with Scherrer's equation are

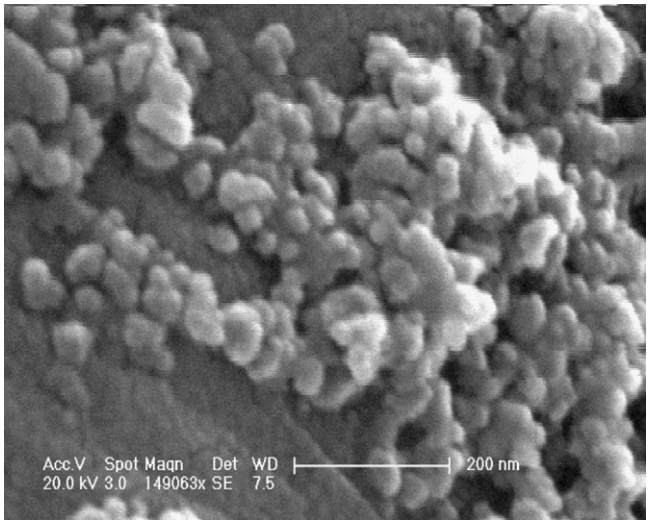

Fig. 3. FESEM micrograph showing typical particle morphology of the 10NDC powder calcined at 700 °C for 4 h.

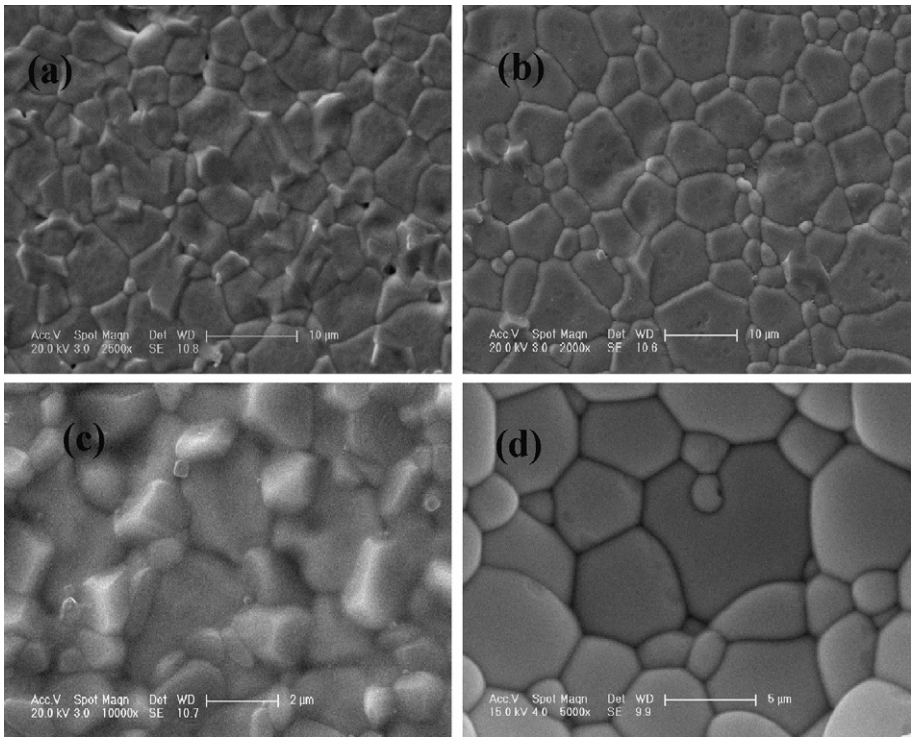

Fig. 4. FESEM micrographs showing the thermal-etched pellets sintered at 1450 °C: (a) 5NDC; (b) 5NDC with Mo doping; (c) 10NDC; (d) 10NDC with Mo doping.

5.7 nm, 9.1 nm and 18.2 nm for 10NDC calcined at 300 °C, 500 °C and 700 °C for 4 h, respectively. The morphology of this powder after being calcined at 700 °C is shown in Fig. 3, and the particle size is between 15 nm and 20 nm. Fig. 2b and c presents the XRD patterns of the undoped-NDC and Mo-doped NDC samples sintered at 1450 °C for 24 h. According to Nitani's report [33], the solubility limit of $NdO_{1.5}$ in CeO_2 was 30%, as we expected, all the undoped-NDC samples are single phases. Furthermore, the XRD patterns of NDC samples with Mo doping did not show the existence of any secondary phase.

Fig. 4 shows the microstructure of the undoped-NDC and Mo-doped NDC samples sintered at 1450 °C. As illustrated in Fig. 4a and c, the undoped-NDC samples show few pores and have relatively uniform grain size distribution. On the other hand, it is observed that grains of NDC with Mo doping (see Fig. 4b and d) are larger. The relatively lower uniformity is probably induced by the increased grain boundary mobility with Mo doping. It has

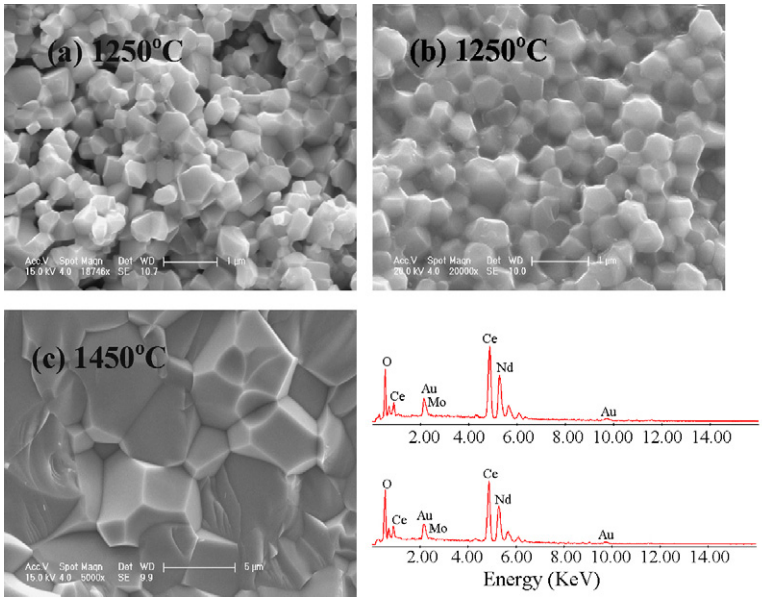

Fig. 5. FESEM showing the cross-section images of 15NDC pellets: (a) 1250 °C without Mo doping; (b) 1250 °C with Mo doping; (c) 1450 °C with Mo doping and the corresponding EDAX spectra (top: bulk; bottom: triple point).

larger grains, i.e. the smaller grain boundary regions, therefore, the smaller grain boundary resistance in the impedance measurement. From the FESEM images shown in Fig. 4, NDC with Mo doping show larger grain sizes than the samples without Mo, which is consistent with the result of NDC with Gallia dopant [34]. Fig. 5 is the FESEM cross-section images of 15NDC pellets sintered at 1250 °C and 1450 °C with and without Mo doping and the corresponding EDAX patterns of the specimen with Mo doping sintered at 1450 °C. It can be seen that the sample with Mo doping (Fig. 5b) has uniform grain size of about 500 nm and the grains are connected to each other with a relative density above 95%, whereas the pellet without Mo doping has many pores after being sintered at 1250 °C with the relative density lower than 80%. With the increase of heating temperature, the grain size increased greatly (Fig. 5c) accompanied by the increasing density. Fig. 5 also displays the representative EDAX profiles of bulk (top) and the triple point (bottom) of Fig. 5c. These figures imply that the composition around triple point is almost the same as that of bulk and the Mo content is about 1.2 mol% compared to the initial content of 5.0 mol% due to the volatilization. Furthermore, from the distinct and clean grain boundaries in images of Figs. 4 and 5, we can conclude that Mo additive distributes uniformly in the sample.

3.2. Electrical properties

The samples for electrical measurement were sintered at 1450 °C for 24 h to ensure a high relative density. The ac

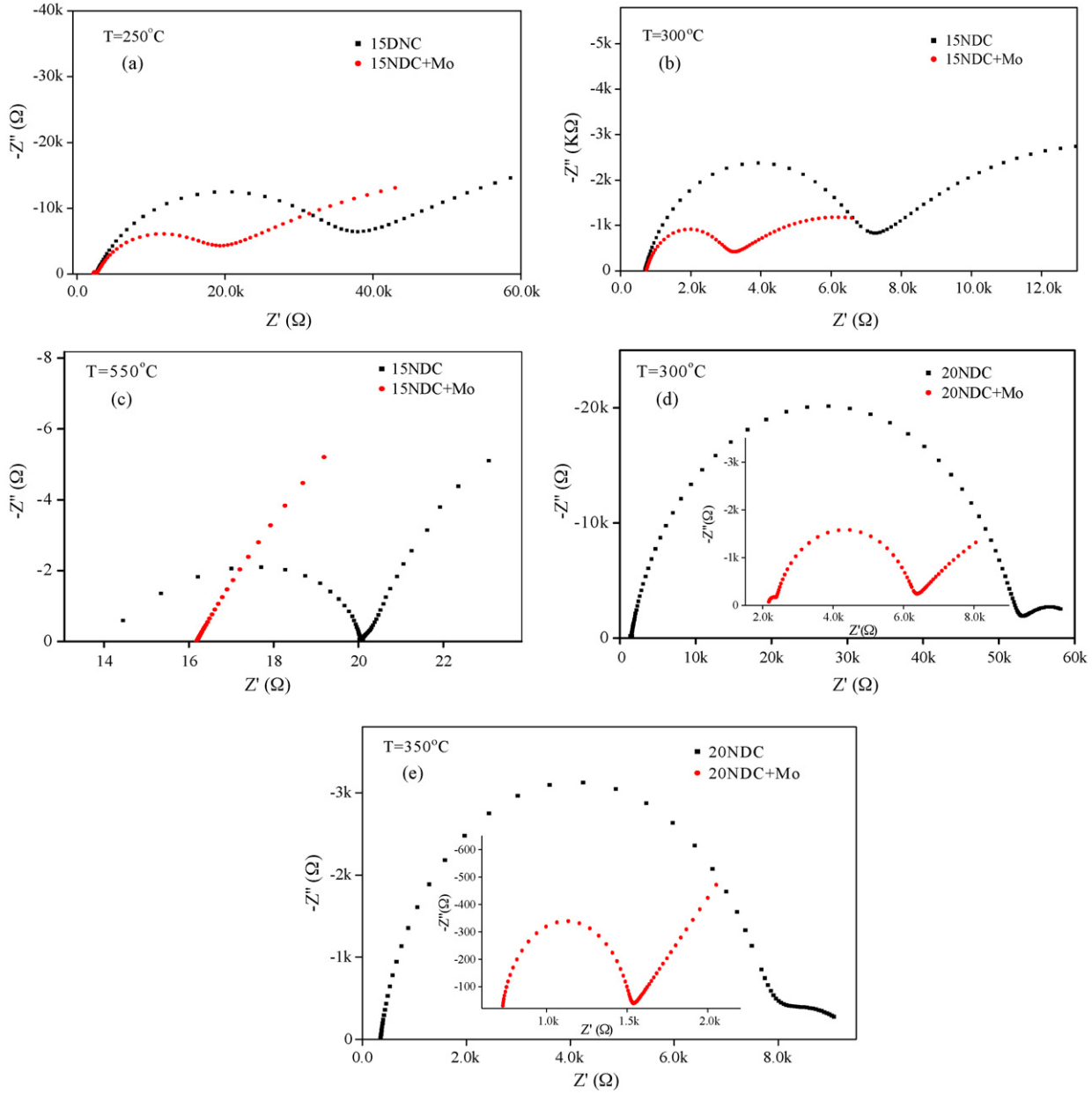

Fig. 6. Impedance spectra of 15NDC (a, b, c) and 20NDC (d, e) sintered at 1450 °C with and without Mo doping at different temperatures in air; the equivalent circuits used in analyzing the impedance spectra (f, g).

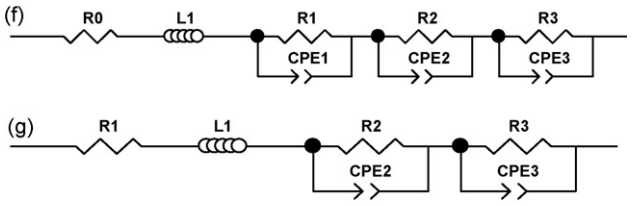

R0: Lead wire resistance

L1: Inductance of the experiment setup

R1: High frequency semicircle resistance (Grain resistance Rb)

CPE1: High frequency semicircle constant phase element

R2: Middle frequency semicircle resistance (Grain boundary resistance Rgb)

CPE2: Middle frequency semicircle constant phase element

R3: Low frequency semicircle resistance (Electrode processes Re)

CPE3: Low frequency semicircle constant phase element

Fig. 6. (*Continued*).

impedance of an ionic conductor measured via a two-probe method contains the contributions of the grain interior, grain boundaries and electrode–electrolyte interfaces at high, middle and low frequencies. They can be represented in a complex plane by three arcs. When the ac measurement was plotted on complex impedance plots (Z'' versus Z', where Z' is the real part and Z'' is the negative imaginary part of the complex impedance), three successive arcs were generally observed. Because of the limited frequency range of the equipment (0.1 Hz–1 MHz) and the character of the sample, not all these three arcs were observed at any temperature. Fig. 6 shows the typical Nyquist representations for NDC with and without Mo doping.

According to the results of Refs. [35,36], it is possible to choose the well-adapted equivalent electrical circuits to fit the impedance spectra of the electrolyte and obtain different resistances R and capacitances C. In Fig. 6, the incomplete or small arc in the high frequency range can be attributed to the grain polarization. The broad arc in the middle frequency range is due to the grain boundary polarization. And the spike appearing in low frequency is ascribed to the electrode polarization. The grain polarization in the high frequency range was from the inductance of the instrument and the test setup. A parallel RC element represents a drop capacitor with a typical relaxation time which corresponds to the process. However, in the present case, in place of capacitor a constant phase element (CPE) is applied to model the experimental data. The CPE is equivalent to a distribution of capacitors in parallel; as such, it accounts for the microstructure inhomogeneity within the sample and it was calculated from the observed impedance spectra using the circuit shown in Fig. 6f and g, in which $R0$, $L1$, $R1$, $R2$, $R3$, CPE1, CPE2 and CPE3 represent the resistance of lead wires (it is considered only at low temperatures, while it can be omitted at high temperatures), inductance of the experiment setup, grain resistance, grain boundary resistance, electrode resistance, constant phase element of the grain, constant phase element of the grain boundary and constant phase element of the electrode, respectively. The general expression of the CPE is $Z = 1/C(j\omega)^n$,

Table 1
Fitting parameters of 20NDC with Mo doping

Parameter	Temperature (°C)													
	250	300	350	400	450	500	550	600	650	700	750	800		
$R0$ (Ω)	2549	0.0008												
$L1$ (10^{-6})	160	150	34	5.80	4.80	3.50	3.47	118	23.8	6.80	19	1.03		
$R1$ (Ω)	7148	2392	712	269	114	55.1	22	14	8	4.97	3.19	2.02		
CPE1 (pF)	361	368												
n	0.88	0.85												
$R2$ (Ω)	20865	3849	812	225	74.1	28.15	19.4	8.96	5.04	3.29	2.28	1.76		
CPE2 (nF)	91.50	119	144	222	308	182	93	7030	8.69	44	129	56.5		
n	0.88	0.87	0.87	0.85	0.83	0.87	0.87	0.81	0.81	0.73	0.24	0.98		
$R3$ (Ω)	51980	11026	8005	3231	400	87.0	33	14.7	8.24	4.73	2.76	1.55		
CPE3 (mF)	0.13	0.47	1.70	4.70	15	37	52	90	130	160	190	230		
n	0.49	0.49	0.49	0.50	0.60	0.75	0.75	0.80	0.84	0.83	0.81	0.79		

where C indicates the ideal capacitance when $n = 1$, $j = (-1)^{1/2}$ and ω shows the angular frequency.

It can be seen from Fig. 6 that the well-resolved arcs for both bulk and grain boundary only exist at very limited temperatures, due to the limited frequency range of the equipment and the temperature dependence of the bulk and grain boundary resistances. With the increase of temperature, the frequency range shifts to a higher value. The relaxation frequency of the grain boundary is significantly lower at the intermediate temperature due to the higher capacitance values. However, at higher temperature (e.g. 550 °C), one cannot distinguish the bulk and the grain boundary conductivities since there is only one lower characteristic frequency term, from which we obtain the sum of the bulk and grain boundary resistance on the onset of the spike (Fig. 6c). Thus, de-convolution of the bulk and the grain boundary contribution is restricted to a limited temperature, which is insufficient to analyze typical bulk and grain boundary resistance of the ceria-based materials. In order to estimate the bulk and grain boundary resistance at higher temperatures, we extrapolated the grain boundary resistance ($R_{gb,ext}$) from the total conductivity to estimate the bulk resistance ($R_b \approx R_t - R_{gb,ext}$), as proposed elsewhere [37–39]. The fitting parameters with the fitting error less than 5% are shown in Table 1, here we only show the sample of 20NDC with Mo doping for clarity.

Fig. 7a shows Arrhenius plots of the total conductivity whereas at high temperature all the plots converged. 15NDC with and without Mo doping show the highest total conductivity ($\sigma_t = 1.19\ S\ m^{-1}$, $1.17\ S\ m^{-1}$ at 600 °C) with the lowest activation energy ($E_t = 0.849$ eV, 0.937 eV) (Table 2). The high conductivity of undoped-15NDC ($\sigma_t = 1.17\ S\ m^{-1}$ at 600 °C) can compare with that of 2% Bi_2O_3-doped ScSZ ($\sigma_t = 1.18\ S\ m^{-1}$) recently reported by Sarat [40] and it is much higher than that of $Bi_2V_{1.9}Cu_{0.1}O_{1.95}$(BICUVOX), $Ce_{0.9}Gd_{0.1}O_{1.95}$(GDC), $La_{0.9}Sr_{0.1}Ga_{0.8}Mg_{0.2}O_{2.85}$(LGSM) and $(ZrO_2)_{0.90}(Y_2O_3)_{0.10}$(YSZ) [41]. Considering the results reported by Ifan and Aneflous [24,25], the dispersed result is probably due to the different impurity especially the SiO_2 content. Recently, Zhang reported that 15GDC shows the highest conductivity instead of 20GDC in high purity systems [20]. In Fig. 7a, the conductivity of the samples with and without Mo doping shows the same trend, i.e. the conductivity increased with increasing Nd_2O_3 content up to 15 mol% and it

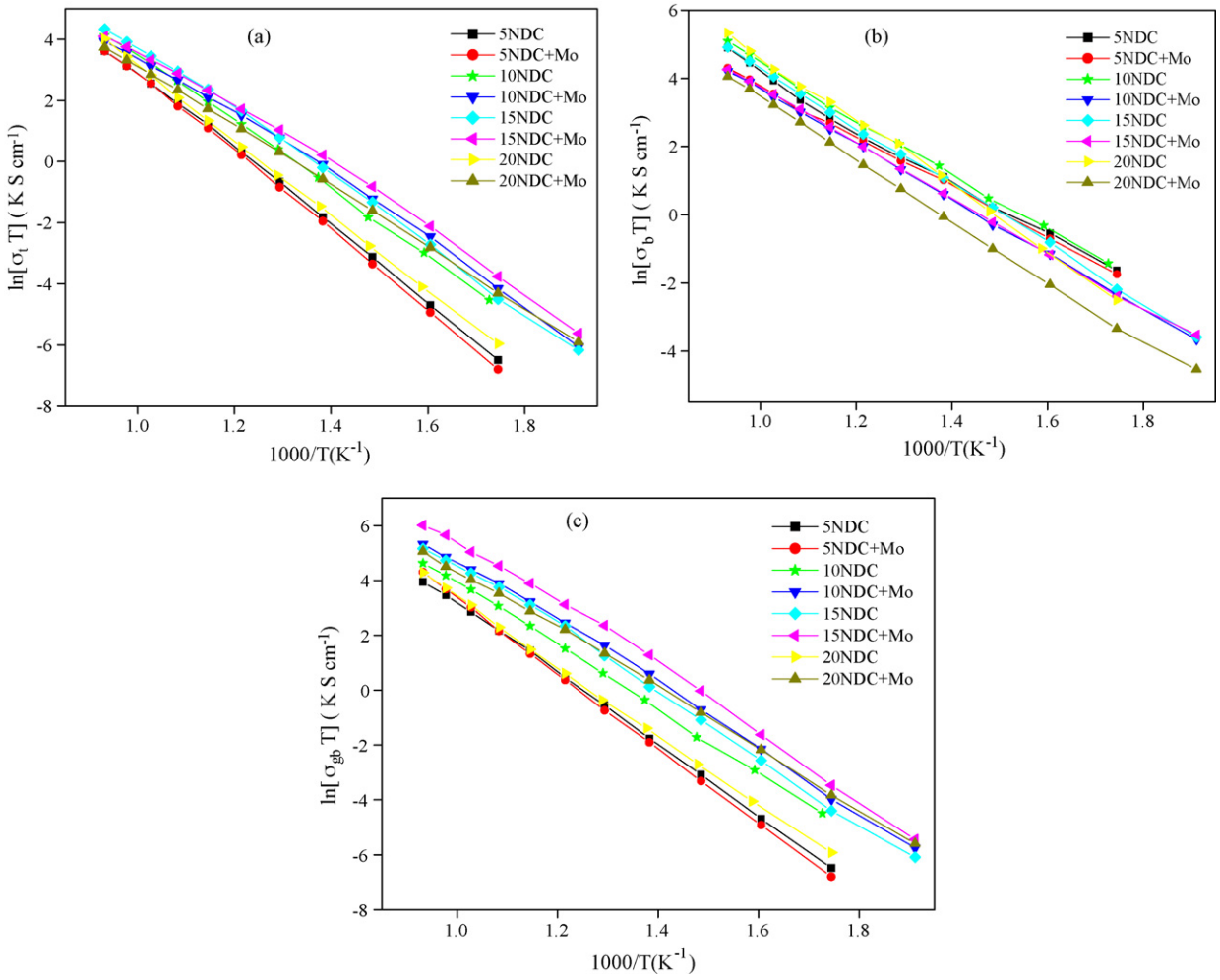

Fig. 7. Arrhenius plots from impedance measurement for NDC with and without Mo doping: (a) total conductivity; (b) bulk conductivity; (c) grain boundary conductivity.

Table 2
Main characteristics of NDC ceramics sintered at 1450 °C for 24 h with and without Mo doping

Sample	Relative density (%)	R_{gb}/R_t (%), 600 °C	$\sigma_{t(600)}$ (S m^{-1})	$\sigma_{b(600)}$ (S m^{-1})	$\sigma_{gb(600)}$ (S m^{-1})	E_t (eV)	E_b (eV)	E_{gb} (eV)
5NDC	97.1	0.799	0.387	1.96	0.484	1.08	0.681	1.12
10NDC	96.9	0.689	0.819	2.65	1.19	0.947	0.705	0.998
15NDC	97.3	0.472	1.17	2.29	2.56	0.937	0.742	1.02
20NDC	97.2	0.861	0.433	3.11	0.506	1.06	0.818	1.09
5NDC + Mo	96.9	0.796	0.342	1.67	0.429	1.11	0.636	1.18
10NDC + Mo	96.8	0.331	0.945	1.41	2.86	0.864	0.696	0.988
15NDC + Mo	97.7	0.209	1.19	1.49	5.62	0.849	0.705	1.02
20NDC + Mo	97.5	0.316	0.642	0.960	2.03	0.852	0.772	0.900

rapidly decreased when the concentration of Nd_2O_3 is further increased. The trend can be explained using Kroeger-Vink notation which could be expressed with following equation:

$$Nd_2O_3 \xrightarrow{CeO_2} 2Nd'_{Ce} + 3O_O + V_O^{\bullet\bullet}$$

where Nd'_{Ce} indicates one Ce^{4+} site occupied by one Nd^{3+} ion. The addition of Nd_2O_3 into the CeO_2 system would lead to the formation of oxygen vacancy because of the charge compensation. In electrolyte materials, the vacancy will attract the doping ions to produce complexes (e.g. $Nd'_{Ce}V_O^{\bullet\bullet}$/$Nd'_{Ce}V_O^{\bullet\bullet}Nd'_{Ce}$) due to the static forces. At lower dopant content, most of these oxygen vacancies $V_O^{\bullet\bullet}$ are probably mobile, which could explain the gradual increase of conductivity. While at higher dopant content, defect associations ($Nd'_{Ce}V_O^{\bullet\bullet}$/$Nd'_{Ce}V_O^{\bullet\bullet}Nd'_{Ce}$) localized near Nd^{3+} begin to form at the expense of oxygen vacancies [42], and the complexes will prevent oxygen vacancies from passing though the lattice and result in the decrease of conductivity.

The bulk conductivity of NDC with and without Mo doping as a function of temperature is shown in Fig. 7b. We can see that 20NDC without Mo doping has the highest conductivity at high temperature and 10NDC has a better one at lower temperature. This result differs from that of Aneflous [25], i.e. σ_b almost reaches a constant value in the range of 10–25 mol% of Nd^{3+}. However, σ_b of all the samples decreased with Mo doping. It is probably due to the dissolution of MoO_3 into the lattice which impedes the move of oxygen vacancy. The similar result has been reported by Zhang et al. [21,22], that for $Ce_{0.9}Gd_{0.1}O_{2-\delta}$ doped by transition oxides (MnO_2, Fe_2O_3 and Co_3O_4), the bulk conductivity also shows a little decrease. It can be seen from the EDAX in Fig. 5, the content of Mo in bulk is almost the same as that of triple grain contacts.

Arrhenius plots of the grain boundary conductivity of NDC with and without Mo doping are shown in Fig. 7c. Note that the conductivity of grain boundary has the same trend as that of the total. This is due to the fact that the grain boundary makes the primary contribution to the total in polycrystalline electrolytes. The conductivity increases obviously as dopant concentration increases and attains the maximum at 15 mol%. However, out of this range, the conductivity reduces as the dopant concentration further increases. 15NDC with and without Mo doping show the highest grain boundary conductivity (σ_{gb} = 5.62 S m^{-1}, 2.56 S m^{-1} at 600 °C, respectively), i.e. the grain boundary conductivity increased more than two times. This can be further approved by the change of grain boundary contribution after Mo doping as shown in Table 2. The lowest dopant content in 5NDC with and without Mo doping results in the lowest conductivities. The similar results related to the grain boundary effect were reported by Gerhardt and Wang [43–45]. By comparing the activation energy of grain and grain boundary in Table 2, we can see that the activation energy of grain is much lower than that of grain boundary. Also we note from Table 2 that the $\Delta E = E_{gb} - E_b$ for 5NDC with and without Mo doping is large (ΔE = 0.543 eV, 0.436 eV, respectively). Gerhardt and Wang reported that grain boundary effect was the greatest for dilute solid solutions and became vanishing for dopant concentrations higher than 15 mol%. The grain boundary resistance of the lower dopant content is greater than the higher dopant content. Accordingly, 5NDC other than higher dopant concentration shows the lowest grain boundary conductivity. Based on the space-charge layer theory as discussed in Refs. [7–9], a grain boundary consists of a grain boundary core and two adjacent space-charge layers at both sides. Negatively charged species (i.e. Nd'_{Ce}) segregate effectively at the grain boundaries, in which positively charged $V_O^{\bullet\bullet}$ are depleted. Therefore, the space-charge layers block $V_O^{\bullet\bullet}$ across the grain boundaries. Tschöpe [46] also reported that a positive space-charge potential was established and resulted in an accumulation of electronic and depletion of ionic charge carriers (positively charged oxygen vacancies) in the screening space-charge layers which were caused by an enhanced oxygen deficiency at grain boundaries.

With Mo doping, the grain boundary and total conductivity increased while the bulk conductivity decreased. Fig. 8 shows the bulk and grain boundary conductivity of 15NDC versus 1/T. We can see that the change of grain boundary is larger than that of bulk resulting in the increase of total conductivity. As mentioned above, the decrease in grain conductivity is probably due to the dissolution of MoO_3 into the lattice of $Ce_{1-x}Nd_xO_{2-x/2}$. The increase in grain boundary conductivity can be mainly ascribed to the increase of grain size. With Mo doping, the grain size increased greatly, which is consistent with the results that the undersized transition oxides could remarkably enhance the mobility of grain boundary in CeO_2 as reported by Chen and Chen [27,28]. The increased grain boundary mobility is probably due to the large distortion of the surrounding lattice that apparently facilitates defect migration of the CeO_2 matrix. When the size of a dopant is much smaller than that of matrix ions, certain asymmetry in lattice distortion will be formed, which leads to faster diffusivity of matrix ions. Chen and Chen [27,28] attribute this phenomenon to the effect of severely undersized dopants. As the size of Mo^{6+} (0.62 Å) is smaller

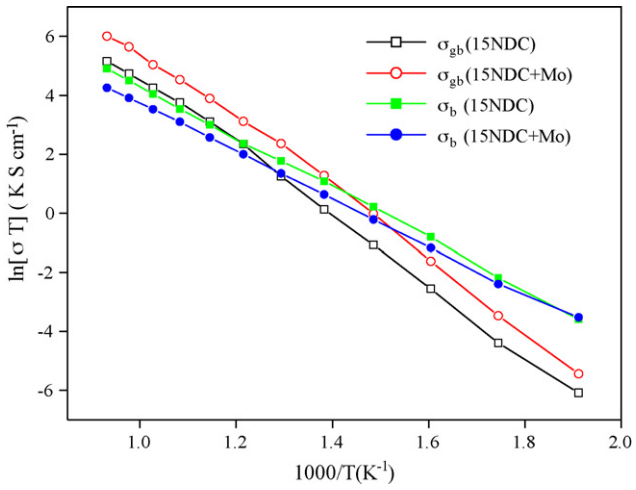

Fig. 8. Arrhenius plots of bulk and grain boundary of 15DNC with and without Mo doping.

than that of matrix ion Ce^{4+} (0.92 Å), this molybdenum oxide will probably promote the grain boundary mobility greatly and result in the increased grain size and decreased sintering temperature. Referring to the FESEM in Fig. 4, the sample with Mo doping has the larger grains, i.e. the smaller grain boundary region, thus, it has the smaller grain boundary resistance in the impedance measurement (Fig. 6) and the higher corresponding grain boundary conductivity. To further understand the electrical properties of Mo-doped NDC system, a deep study of some parameters such as the optimal content of molybdenum oxide, appropriate sintering temperature and time, the exact form of molybdenum oxide because of the multivalence and the high volatility of molybdenum system is necessary. Those works are now in progress.

4. Conclusion

We have successfully synthesized the solid solutions of high purity $Ce_{1-x}Nd_xO_{2-x/2}$ ($0.05 \le x \le 0.2$) by a modified sol–gel method. 15NDC sample shows the highest total and grain boundary conductivity ($\sigma_t = 1.17\,S\,m^{-1}$, $\sigma_{gb} = 2.5\ 6\,S\,m^{-1}$, 600 °C). While 5NDC shows the lowest conductivity ($\sigma_t = 0.387\,S\,m^{-1}$, $\sigma_{gb} = 0.484\,S\,m^{-1}$, 600 °C) with the highest activation energy ($E_t = 1.08$ eV, $E_{gb} = 1.12$ eV), which could be successfully interpreted by the grain boundary effect.

With Mo doping, the grain boundary conductivity increased notably especially at intermediate and lower temperatures, and the sintering temperature decreased for about 200 °C. We convince that molybdenum oxide has the same trend to enhance the grain boundary mobility as other transition oxides as concluded from the decreased sintering temperature and the increased grain size.

Acknowledgments

This work was financially supported by National Natural Science Foundation of China (grant nos. 20331030, 20671088, 20661026).

References

[1] N.Q. Minh, J. Am. Ceram. Soc. 76 (1993) 563–588.
[2] H. Inaba, H. Tagawa, Solid State Ionics 83 (1996) 1–16.
[3] T.H. Etshell, S.N. Flengas, Chem. Rev. 70 (1970) 339–376.
[4] B.C.H. Steel, A. Heinzel, Nature 414 (2001) 345–352.
[5] H. Yahiro, K. Eguchi, H. Arai, Solid State Ionics 36 (1989) 71–75.
[6] I. Riess, D. Braunshtein, D.S. Tannhauser, J. Am. Ceram. Soc. 64 (1981) 479–485.
[7] J. Maier, B. Bunsenges, Phys. Chem. 90 (1986) 26–33.
[8] X. Guo, Solid State Ionics 96 (1997) 247–254.
[9] X. Guo, W. Sigle, J. Maier, J. Am. Ceram. Soc. 86 (2003) 77–87.
[10] B.C.H. Steele, Solid State Ionics 129 (2000) 95–110.
[11] T.S. Zhang, J. Ma, S.H. Chan, P. Hing, J.A. Kilner, Solid State Sci. 6 (2004) 565–572.
[12] S.P.S. Badwal, Solid State Ionics 76 (1995) 67–80.
[13] M.J. Verkerk, B.J. Middelhuis, A.J. Burgraaf, Solid State Ionics 6 (1982) 159–170.
[14] X.D. Zhou, W. Huebner, I. Kosacki, H.U. Anderson, J. Am. Ceram. Soc. 85 (2002) 1757–1762.
[15] M. Aoki, Y.M. Chiang, I. Kosacki, L.J. Lee, H. Tuller, Y. Liu, J. Am. Ceram. Soc. 79 (1996) 1169–1180.
[16] J. Ma, T.S. Zhang, L.B. Kong, P. Hing, S.H. Chan, J. Power Sources 132 (2004) 71–76.
[17] T.S. Zhang, J. Ma, L.H. Luo, S.H. Chan, J. Alloy Compd. 422 (2006) 46–52.
[18] T.S. Zhang, J. Ma, Y.Z. Chen, L.H. Luo, L.B. Kong, S.H. Chan, Solid State Ionics 177 (2006) 1227–1235.
[19] T.S. Zhang, J. Ma, L.B. Kong, S.H. Chan, P. Hing, J.A. Kilner, Solid State Ionics 167 (2004) 203–207.
[20] T.S. Zhang, J. Ma, H. Cheng, S.H. Chan, Mater. Res. Bull. 41 (2006) 563–568.
[21] T.S. Zhang, J. Ma, S.H. Chan, J.A. Kilner, Solid State Ionics 176 (2005) 377–384.
[22] T.S. Zhang, J. Ma, Y.J. Leng, S.H. Chan, P. Hing, J.A. Kilner, Solid State Ionics 168 (2004) 187–195.
[23] D. Pérez-Coll, P. Núñez, J.C.C. Abrantes, D.P. Fagg, V.V. Kharton, J.R. Frade, Solid State Ionics 176 (2005) 2799–2805.
[24] E.L. Ifan, Stephens, J.A. Kilner, Solid State Ionics 177 (2006) 669–676.
[25] L. Aneflous, J.A. Musso, S. Villain, J.R. Gavarri, H. Benyaich, J. Solid State Chem. 177 (2004) 856–865.
[26] X.M. Lin, L.P. Li, G.S. Li, W.H. Su, Mater. Chem. Phys. 69 (2001) 236–240.
[27] P.L. Chen, I.W. Chen, J. Am. Ceram. Soc. 76 (1993) 1577–1583.
[28] P.L. Chen, I.W. Chen, J. Am. Ceram. Soc. 79 (1996) 1793–1800.
[29] C.D.E. Lakeman, D.A. Payne, Mater. Chem. Phys. 38 (1994) 305–324.
[30] C. Marcilly, P. Courty, B. Delmon, J. Am. Ceram. Soc. 53 (1970) 56–57.
[31] H.P. Klug, L.E. Alexander, X-ray Diffraction Procedures for Polycrystalline and Amorphous Materials, Wiley–Interscience, New York, 1974, p. 540.
[32] M.I. Mendelson, J. Am. Ceram. Soc. 52 (1967) 443–446.
[33] H. Nitani, T. Nakagawa, M. Yamanouchi, T. Osuki, M. Yuya, T.A. Yamamoto, Mater. Lett. 58 (2004) 2076–2081.
[34] H. Yoshida, K. Miura, T. Fukui, S. Ohara, T. Inagaki, J. Power Sources 106 (2002) 136–141.
[35] J.V. Herle, D. Seneviratne, A.J. McEvoy, J. Eur. Ceram. Soc. 19 (1999) 837–841.
[36] J.V. Herle, R. Vasquez, J. Eur. Ceram. Soc. 24 (2004) 1177–1180.
[37] D. Pérez-Coll, P. Núñez, J.R. Frade, J. Electrochem. Soc. 153 (3) (2006) A478–A483.
[38] D. Pérez-Coll, D. Marrero-López, P. Núñez, S. Piñol, J.R. Frade, Electrochim. Acta 51 (2006) 6463–6469.
[39] D. Pérez-Coll, P. Núñez, J.C. Ruiz-Morales, J. Apeña-Martínez, J.R. Frade, Electrochim. Acta 52 (2007) 2001–2008.
[40] S. Sarat, N. Sammes, A. Smirnova, J. Power Sources 160 (2006) 892–896.

[41] S.J. Skinner, J.A. Kilner, Mater. Today 6 (3) (2003) 30–37.
[42] L.P. Li, G.S. Li, J. Xiang, R.L. Smith Jr., H. Inomata, Chem. Mater. 15 (2003) 889–898.
[43] R. Gerhardt, A.S. Nowick, J. Am. Ceram. Soc. 69 (1986) 641–646.
[44] R. Gerhardt, A.S. Nowick, M.E. Mochel, I. Dumler, J. Am. Ceram. Soc. 69 (1986) 647–651.
[45] D.Y. Wang, A.S. Nowick, J. Solid State Chem. 35 (1980) 325–333.
[46] A. Tschöpe, R. Birringer, J. Electroceram. 7 (2001) 169–177.